JACS Au
AN OPEN ACCESS JOURNAL OF THE AMERICAN CHEMICAL SOCIETY

Open Access
This article is licensed under CC-BY-NC-ND 4.0

pubs.acs.org/jacsau
Article

Nature of the Active Center for the Oxygen Reduction on Ag-Based Single-Atom Alloy Clusters

Yixuan Pu,[§] Jia-Lan Chen,[§] Jian-Wen Zhao, Li Feng, Jinze Zhu, Xuechun Jiang, Wei-Xue Li, and Jin-Xun Liu*

Cite This: *JACS Au* 2024, 4, 2886−2895
Read Online
ACCESS | Metrics & More | Article Recommendations | Supporting Information

ABSTRACT: The development of alternative alloy catalysts with high activity, surpassing platinum group metals, for the oxygen reduction reaction (ORR) is urgently needed in the field of electrocatalysis. The Ag-based single-atom alloy (AgSAA) cluster has been proposed as a promising catalyst for the ORR; however, enhancing its activity under operational conditions remains challenging due to limited insights into its actual active site. Here, we demonstrate that the operando formation of the $MO_x(OH)_y$ complex serves as the key active site for catalyzing the ORR over AgSAA cluster catalysts, as revealed through comprehensive neural network potential molecular dynamics simulations combined with first-principles calculations. The volcano plot of the ORR over the $MO_x(OH)_y$ complex addresses the gaps inherent in traditional metallic alloy models for pure AgSAA cluster catalysts in ORR catalysis. The appropriate orbital hybridization between OH and the dopant metal in the $MO_x(OH)_y$ complexes indicated that the $Ag_{54}Co_1$, $Ag_{54}Pd_1$, and $Ag_{54}Au_1$ clusters are optimal AgSAA catalysts for the ORR. Our work underscores the significance of theoretical modeling considering the reaction atmosphere in uncovering the true active site for the ORR, which can be extended to other reaction systems for rational catalyst design.

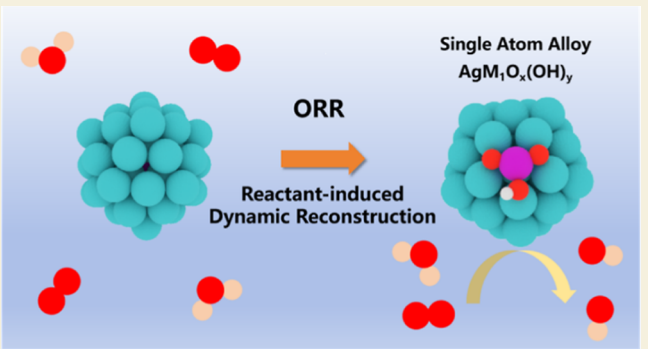

KEYWORDS: *alloy, catalysts, ORR, AgSAA, cluster*

INTRODUCTION

Renewable energy conversion and storage technologies, such as water electrolyzers, batteries, and fuel cells, have garnered widespread attention and interest in recent years, driven by the goal of establishing a clean and sustainable society. At the heart of numerous energy conversion and storage systems is the oxygen reduction reaction (ORR), which plays a vital role in the functionality and efficiency of these systems.[1,2] Currently, there has been a renewed focus on ORR catalysts in alkaline environments due to the lower adsorption energies of anions and the enhancement of ORR kinetics under such conditions.[3−6] Platinum group metals (PGMs)[7,8] have traditionally served as standard catalysts for the ORR in alkaline media; however, the high cost associated with PGM limits their practical application.[9] Consequently, the exploration and development of alternative nonnoble metal-based catalysts demonstrating higher activity than PGM for the ORR have emerged as significant and innovative fields within the realm of electrocatalysis.[10,11] Advancing the frontier of ORR investigations involves the engineering of nanostructures in multimetallic alloys and clusters[12] to enhance their activity and stability by fine-tuning the electronic and geometric structures, as well as leveraging synergistic effects.

Silver (Ag) metal, which is abundant and cost-effective, is considered a potential alternative to expensive catalysts for the ORR in alkaline environments over Pt-based catalysts. Numerous silver nanoalloys, including AgPd, AgCu, and AgCo nanoalloys, have been reported in experiments because of their efficient electrocatalytic performance in facilitating the ORR in alkaline fuel cells and batteries.[13,14] Density functional theory (DFT) calculations revealed that Mn, Fe, Co, Zr, Mo, and W are particularly effective ORR catalysts when incorporated into Ag_3M mixed-surface nanoalloys.[15] Single-atom alloys (SAAs) are a new class of single-site alloy catalysts that feature small quantities of isolated metal atoms dispersed within more inert and catalytically selective host metals.[16,17] The unique electronic structure of SAA, coupled with the synergistic effect between the doped single atom and the host metal, has the potential to enhance catalytic activity and

Received: February 6, 2024
Revised: July 22, 2024
Accepted: July 22, 2024
Published: July 26, 2024

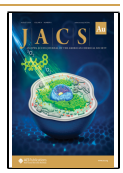

© 2024 The Authors. Published by American Chemical Society

https://doi.org/10.1021/jacsau.4c00116
JACS Au 2024, 4, 2886−2895

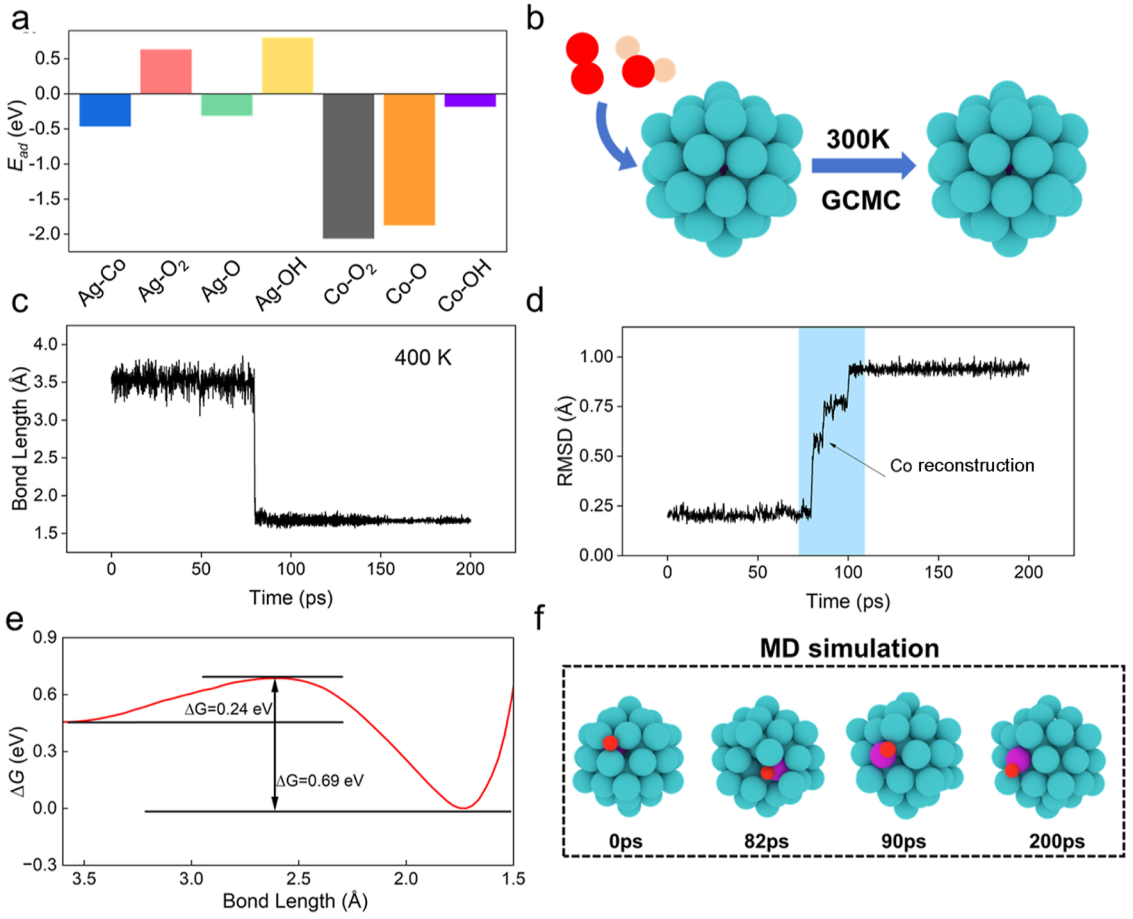

Figure 1. Adsorption energetics and dynamic behavior of the $Ag_{54}Co_1$ cluster. (a) Calculated adsorption energies of O*/O_2* and OH* species at the surface Ag site and Co site of the $Ag_{54}Co_1$ cluster with respect to gaseous O_2 and OH^- in solution, respectively. The cohesive energy between Co and Ag in the $Ag_{54}Co_1$ cluster was also calculated based on the equation $Ag_{55} + Co_1(bulk) \rightarrow Ag_{54}Co_1 + Ag_1(bulk)$. All the energies are in eV. (b) GCMC simulation to identify the number of adsorbed O* or OH* species on the $Ag_{54}Co_1$ cluster. The surface-adsorbed O* can be transformed into OH*, which was calculated based on the reaction $O^* + H_2O + e^- \rightarrow OH^* + OH^-$. The Gibbs free energy of OH^- in solution was calculated as $G_{OH} = 1/4\ (2G_{H_2O} + G_{O_2} - 4.92)$. (c) ML-accelerated MD simulations conducted to study the adsorption of O* on the $Ag_{54}Co_1$ cluster for 200 ps at 400 K. (d) rmsd of $Ag_{54}Co_1$ during MDs over 0.2 ns. (e) Free energy surface (FES) of Co atom migration from the inside to the surface of the $Ag_{54}Co_1$ cluster calculated by metadynamics, with the collective variable being the bond length between Co and O atoms. (f) Snapshot of the ML-accelerated MD simulation depicting O* adsorption on the $Ag_{54}Co_1$ cluster. The blue, pink, red, and orange spheres represent Ag, Co, O, and H atoms, respectively.

selectivity in many chemical reactions compared to each counterpart of the catalysts.[18−21] These features, including high catalytic activity, exceptional selectivity, and reduced material consumption, position SAA as a promising catalyst candidate for various reactions.[16,17,22−27] In particular, incorporating isolated atoms such as Ni, Pd, Pt, Co, and Rh into Ag(111) and Au(111) matrices significantly enhances the catalytic performance of SAA catalysts by promoting optimal adsorption configurations for intermediates such as O_2*, OOH*, O*, and OH*.[28] The Ag-based SAA (AgSAA) cluster functions as an innovative catalyst for the ORR. Gold−silver alloy nanoclusters composed of $Ag_{21}Au_1$ SAA supported on activated carbon exhibited outstanding ORR activity in alkaline solutions.[29] Additionally, an exceptional ORR performance is attainable with Ag clusters/nanoparticles that are even doped with a small number of Cu atoms.[30,31] Further theoretical studies indicate that the $Ag_{12}Cu_1$ alloy cluster is a more effective ORR catalyst than the Ag_{13} and Cu_{13} clusters.[32] Despite many investigations, the determination of the optimal catalyst and the understanding of the actual active sites and the catalytic role of AgSAA cluster catalysts under operational conditions for the ORR are open questions that hinder rational catalyst design.

For a specific AgSAA cluster catalyst, the surface composition and structure undergo dynamic changes due to competition between the reactant/intermediate and metallic atoms in the AgSAA cluster in response to the reaction atmosphere. Therefore, identifying the surface structure and active site of AgSAA clusters for the ORR remains a highly challenging task from experimental and theoretical modeling points of view. Herein, we performed comprehensive theoretical modeling to reveal the catalytic role of AgSAA clusters in the ORR in aqueous alkaline media. The representative magic-numbered $Ag_{54}Co_1$ clusters (~1.1 nm) were studied extensively in the present work. Grand canonical Monte Carlo (GCMC) simulations demonstrated that the $Ag_{54}Co_1$ cluster is in the metallic phase and that a single Co atom resides in the core of the $Ag_{54}Co_1$ cluster in aqueous alkaline solution. However, neural network potential molecular dynamics (MD) simulations combined with ab initio thermodynamic analysis have shown that atomic oxygen intermediates can induce the migration of Co atoms onto Ag

https://doi.org/10.1021/jacsau.4c00116
JACS Au 2024, 4, 2886−2895

surfaces during the formation of Co_1O_2OH complexes. The operando formation of the $MO_x(OH)_y$ complex can also be found in other $Ag_{54}M_1$ (M = Co, Ni, Fe, Ru, Rh, Pd, Pt, Au, Cu, Zn, and In) cluster systems. The volcano plot for the ORR, based on the $MO_x(OH)_y$ complex, validates previous experimental measurements, which cannot be understood by conventional pure metallic $Ag_{54}M_1$ cluster models. The $M_1O_x(OH)_y$ complex formed under operating conditions can be the actual active site for the ORR. We predicted that the most active $Ag_{54}Co_1$, $Ag_{54}Pd_1$, and $Ag_{54}Au_1$ could be promising AgSAA cluster catalysts for the ORR. The formation of stable $MO_x(OH)_y$ complexes in an AgSAA catalyst under the conditions of the ORR suggests that complex surface chemistry is likely common, challenging the simplicity of conventional metallic AgSAA models. Our work may prompt a reconsideration of the active site of SAA catalysts for various other reactions.

RESULTS AND DISCUSSION

DFT calculations were first performed to study the stability of the "magic-numbered" 55-atom SAA $Ag_{54}Co_1$ cluster, which was chosen here because it has a diameter of approximately 1.1 nm, in line with the commonly synthesized cluster size in experiments.[33] Additionally, according to the Gibbs−Thomson equation,[34] a 3 nm Ag nanoparticle (0.17 eV) exhibits similar stability to that of a Ag_{55} cluster (0.18 eV). Thus, the Ag_{55} cluster demonstrates high stability and can coexist with the nanoparticles, as shown in Figure S1.

A single cobalt atom tends to reside within the core of the $Ag_{54}Co_1$ cluster rather than on its surface at −0.46 eV (Table S1). Consequently, significantly fewer cobalt atoms are present on the surface of the $Ag_{54}Co_1$ cluster. Neural network potential MD simulations revealed that the presence of solvent water neither adsorbed nor induced Co migration from the subsurface to the surface of the $Ag_{54}Co_1$ cluster in 1 ns, indicating a negligible solvent effect in this context (Figure S2). Considering that the kinetic limiting step for the ORR on Ag catalysts is the initial endothermic reduction of O_2, resulting in the formation of an adsorbed OOH* intermediate, our study focused on examining O_2*, O*, and OOH* on the $Ag_{54}Co_1$ cluster. On the surface of the $Ag_{54}Co_1$ cluster, only the key intermediate O* can adsorb slightly exothermically by −0.31 eV, whereas the other O_2* and OH* intermediates prefer to desorb rather than adsorb by 0.63 and 0.80, respectively (Figures 1a and S3). GCMC simulations, with the chemical potential of gaseous O_2 as the sole input, were utilized to quantify the O* species adsorbed on the surface of the $Ag_{54}Co_1$ SAA cluster, as depicted in Figure 1b. From the multitude of DFT calculations for more than 200 structures, the GCMC simulation indicates that the atomic O* species have a low ability to adsorb onto the $Ag_{54}Co_1$ cluster due to the endothermic Gibbs free adsorption energy of 0.17 eV at 273 K. Additionally, the hydrogenation of the O* species to form OH* species is less favorable, as indicated by the endothermic nature of the reaction of $O^* + H_2O + e^- \rightarrow OH^* + OH^-$, with a Gibbs free energy change of 0.13 eV (Table S2). As a result, the clean metallic $Ag_{54}Co_1$ cluster is the most stable configuration without OH* or OH* adsorption under ORR operating conditions from a static theoretical modeling perspective. Our calculations are in line with a previous study indicating that the Ag surface retains its metallic nature under ORR conditions when the potential remains below 0.90 V.[35]

To assess the likelihood of Co migrating from the core to the surface of the $Ag_{54}Co_1$ cluster influenced by adsorbates, we conducted further studies on the adsorption of intermediates O_2*, O*, and OH* on the $Ag_{54}Co_1$ cluster with the Co atom positioned at the surface. Our findings indicate that the calculated adsorption energies of O_2* and O* at the Co atom site are −2.06 and −1.87 eV, respectively (Table S1), which exceed the energy difference for the Co atom in the core and on the surface of the $Ag_{54}Co_1$ cluster. As a result, the strong adsorption of the O_2* and O* atoms at the Co site can thermodynamically facilitate the migration of Co atoms from the core to the surface of the $Ag_{54}Co_1$ cluster. In contrast, the strength of OH* adsorption at the Co atom site (E_{OH} = −0.18 eV) is insufficient to offset the energy cost associated with the migration of the Co atom from the core to the surface of the $Ag_{54}Co_1$ cluster.

Neural network potential MD simulations at 400 K were conducted to explore the likelihood of the dynamic migration of Co from the core to the surface of the $Ag_{54}Co_1$ cluster, a process driven by the adsorption of O_2* and O*, even though this migration is allowed from a thermodynamic perspective. A higher temperature of 400 K was selected as an alternative to room temperature to accelerate the MD simulation. Simultaneously, the adsorbed intermediate O_2* species on Ag atoms cannot drive the migration of subsurface Co to the cluster surface because the considerable distance between the O_2* species and the cluster surface exceeds 3.20 Å, resulting in a strong steric effect preventing O_2* from coming into contact with the Co atom in the core of the $Ag_{54}Co_1$ cluster. However, the chemisorbed O* species could drive the migration of subsurface Co atoms toward the surface of the $Ag_{54}Co_1$ cluster (Figure 1c,d). In the root-mean-square deviation (rmsd) analysis of the whole cluster, we found that before 75 ps, Co atoms were located within the inner cluster and the rmsd was 0.25 Å. From 75 to 110 ps, the Co atom migrated from the inner cluster to the surface and combined with surface oxygen atoms, causing the rmsd to change from 0.25 to 1.0 Å. After 120 ps, the Co atom stabilized at the surface, and the rmsd for the whole $Ag_{54}Co_1O_1$ cluster remained at 1.00 Å (Figure 1d). Further RDF analysis indicated that Ag−Ag and Ag−Co interactions are similar in the first neighbor at 2.5 Å during the 200 ps MD simulations. However, the first neighbor of Co−O is at 1.70 Å after the Co atom migrates to the $Ag_{54}Co_1O_1$ surface (Figure S4). The dynamic migration of Co atoms from the interior to the surface of the $Ag_{54}Co_1$ cluster can be attributed to the low coordination number of Ag atoms within the SAA $Ag_{54}Co_1$ cluster, which allows for atom fluidity and facilitates the feasible movement of subsurface Co atoms toward the cluster surface to adsorb O* during the formation of more stable $Ag_{54}Co_1O_x$ complexes. We performed metadynamic simulations to determine the energy barrier for the migration of Co atoms with a value of 0.24 eV (Figure 1e). This indicates that the migration process is spontaneous even at room temperature. Furthermore, once migration is complete, the Co atom becomes stably anchored on the cluster surface, as returning it to the core would require overcoming a significant energy barrier of 0.69 eV (Figure 1e).

Given the migration of the Co atom from the core to the surface of the cluster, more O* and/or OH* can adsorb at the Co site. We further performed ab initio thermodynamic analysis to determine the number of O* atoms (x) or OH* species (y) involved in the formation of $Ag_{54}Co_1O_x(OH)_y$

https://doi.org/10.1021/jacsau.4c00116
JACS Au 2024, 4, 2886−2895

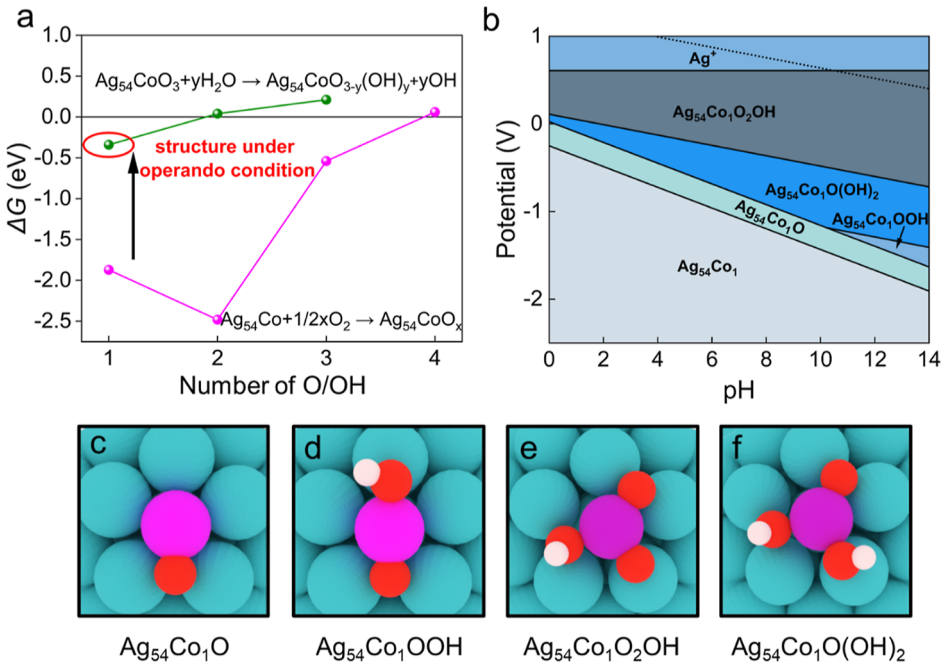

Figure 2. Stability of $Co_1O_x(OH)_y$ complexes. (a) Phase diagram of $Co_1O_x(OH)_y$ complexes obtained by ab initio thermal dynamic analysis. (b) Pourbaix plot of the Co−H_2O system as a function of potential and pH. The ability to form Ag cations was calculated with respect to Ag in the bulk phase. (c−f) Configurations of $Co_1O_x(OH)_y$ complexes. The blue, pink, red, and white spheres are Ag, Co, O, and H atoms, respectively.

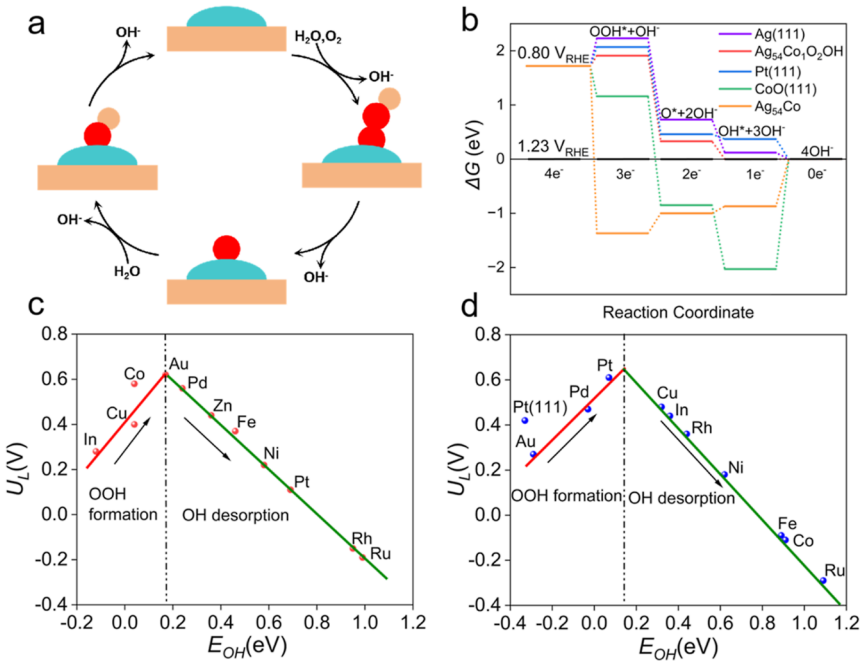

Figure 3. ORR mechanism study. (a) Scheme of the ORR mechanism. The red and orange spheres are O and H atoms, respectively. (b) Potential energy diagram for the ORR over the $Ag_{54}Co_1O_2OH$, $Ag_{54}Co_1$, Ag(111), Pt(111), and CoO(111) surfaces. (c) Volcano plot of the U_L of the $M_1O_x(OH)_y$ complexes formed under operational ORR conditions. (d) Volcano plot of the U_L of the metallic Pt(111) surface and $Ag_{54}M_1$ cluster, where a single M atom is located on the surface of the cluster.

clusters under operating ORR conditions based on the following equation

$$Ag_{54}Co_1 + (x/2 + y/2)O_2 + yH_2O + ye^- \rightarrow Ag_{54}Co_1O_x(OH)_y + yOH^- \quad (5)$$

As the quantity of oxygen atoms increased, the average binding strength of each atomic oxygen gradually weakened (Figure 2a). Consequently, the O* and/or OH* species could adhere to the Co atom site during the formation of $Co_1O_x(OH)_y$ complexes until the ΔG value reached a positive threshold. Interestingly, the Co atom tends to accommodate three oxygen atoms (Co_1O_3) before the change in Gibbs free energy for further addition of oxygen species becomes positive. Moreover, the adsorbed O* species were observed to react with water, resulting in the exothermic formation of adsorbed

https://doi.org/10.1021/jacsau.4c00116
JACS Au 2024, 4, 2886−2895

OH* species. Our observations indicate that one or two adsorbed O* species could undergo a transformation into an OH* species during the formation of the most stable Co_1O_2OH or $Co_1O_1(OH)_2$ configurations under operando ORR conditions (Figure 2a and Table S3).

The evaluation of the stability of $Co_1O_x(OH)_y$ complexes under ORR conditions necessitates consideration of factors such as the pH and voltage under the reaction conditions. A Pourbaix diagram serves as an ideal tool for analyzing this scenario.[36] The calculated Pourbaix diagram (Figure 2b) illustrates potential $Co_1O_x(OH)_y$ structures within the SAA $Ag_{54}Co_1$ cluster system. Co_1O_2OH and $Co_1O(OH)_2$ complexes primarily exist within the alkaline domain (pH > 10) with negative voltages ($V < 0$), while pure metallic $Ag_{54}Co_1$ exhibits greater stability at lower potentials. In contrast, Co_1O_2OH demonstrates greater stability at a higher potential of 0.80 V at pH = 14, which aligns with real basic industrial manufacturing conditions.[37] Therefore, Co_1O_2OH complexes dynamically form during the operando ORR (Figure 2c–f), setting them apart from what is typically considered to occur on the pure metallic SAA $Ag_{54}Co_1$ cluster.

In this study, we focused on the ORR activity over $Ag_{54}Co_1O_2OH$ clusters and found that the inclusion of a graphene support and implicit water led to negligible changes of less than 0.15 eV in the ORR energy landscape (Figure S5). This minimal impact justifies our approach of using the $Ag_{54}Co_1O_2OH$ cluster to explore the intrinsic catalytic behaviors. The ORR mechanism was extensively studied for the identified most stable Co_1O_2OH complexes in alkaline solution (Figure 3a). We used the ORR occurring over the Pt(111), Ag(111), and CoO(111) surfaces as reference points as these are commonly employed in ORR studies. The ORR follows a four-electron process to generate hydroxyl groups (OH^-) in an alkaline solution. Throughout this reaction, the formation of *OOH (a peroxide intermediate) and the subsequent desorption of *OH are commonly regarded as the rate-determining steps in the ORR mechanism.[38] To achieve high ORR activity, an effective catalyst should establish a moderate binding strength with OOH* and OH* intermediates, avoiding both excessive affinity and weak interactions. The Gibbs free energy for the formation of the OH* intermediate (ΔG_{OOH}) on the Pt(111) surface is endothermic at 0.35 eV, whereas a ΔG_{OH} value of −0.36 eV indicates a decreased poisoning effect on the adsorption of OH* on the Pt(111) surface (Figure 3b and Table S2). However, the Ag(111) surface exhibited lower activity than the Pt(111) surface, which was primarily attributed to the greater positive formation energy of the OOH* intermediates on the former surface by 0.51 eV (Table S2). In contrast, the CoO(111) surface also displays much lower activity than the Pt(111) surface due to significantly stronger OH* adsorption ($\Delta G_{OH} = -2.01$ eV), leading to surface poisoning. Finally, the Co_1O_2OH complex could exhibit exceptional ORR activity, as it moderately adsorbed the OOH*/O*/OH* intermediates, distinguishing itself from both the Ag(111) and CoO(111) surfaces (Figure 3b and Table S2).

We calculated the U_L value for the ORR across the four surfaces under consideration. The theoretical limiting potential U_L of the ORR is defined as

$$U_L = -(\max(\Delta G_1, \Delta G_2, \Delta G_3, \Delta G_4))/e \quad (6)$$

where ΔG_1, ΔG_2, ΔG_3, and ΔG_4 are the Gibbs free energy differences at each step of the reaction. This U_L signifies the external voltage needed for each step of the reaction to become spontaneous and is a pivotal measurement for evaluating the catalyst reactivity. The U_L of the Co_1O_2OH complex was measured at 0.61 eV, surpassing that of both the Ag(111) (measured at 0.29 eV) and CoO(111) surfaces (measured at −1.24 eV), as well as that of Pt(111) (measured at 0.45 eV) (Figure S6). Consequently, the Co_1O_2OH complex exhibited superior ORR activity compared with those of the Pt(111), Ag(111), and CoO(111) surfaces. Compared with the Ag_{55} cluster and the Ag(111) surface, the $Ag_{54}Co_1O_2OH$ alloy cluster exhibits enhanced ORR activity, underscoring the critical role of alloy formation in enhancing the ORR performance. This finding clearly demonstrates that the superior catalytic efficiency of the $Ag_{54}Co_1$ alloy cluster is primarily due to the presence and interaction of a single Co atom within the cluster rather than the Ag atoms themselves. Therefore, experimentally synthesizing $Ag_{54}Co_1$ alloy clusters is highly desirable for enhancing the ORR activity (Figure S6 and Table S4). Therefore, $Ag_{54}Co_1$ clusters could be promising candidates for catalyzing the ORR under alkaline conditions, primarily due to the presence and notable reactivity of the Co_1O_2OH complex.

To investigate the universality behind the formation of Co_1O_2OH under ORR conditions, we further examined the stability of the other 10 $Ag_{54}M_1$ clusters (where M represents various elements, namely, Fe, Ni, Ru, Rh, Pd, Pt, Au, Cu, Zn, and In) under ORR conditions. Metadynamics simulations at 400 K for 2 ns revealed the dynamic migration of the investigated single atoms from the core to the surface within the SAA $Ag_{54}M_1$ clusters, which suggested a common pattern in the behavior of these doped single atoms in $Ag_{54}M_1$ SAA clusters, leading to the formation of $M_1O_x(OH)_y$ complexes under ORR conditions driven by strongly adsorbed O* species at the M_1 site (E_O = −0.66 to −1.91 eV; Table S5). The number of O* and OH* groups in the operationally generated $M_1O_x(OH)_y$ complexes was determined by the same method as that used for Co_1O_2OH, as discussed above (Tables S5 and S6 and Figures S7 and S8).

The reconstruction observed in the $Ag_{54}M_1$ cluster during the generation of $M_1O_x(OH)_y$ complexes inspired us to further explore the actual active sites under the ORR conditions (Tables S7–S9). The concept of a volcano plot, well established in the context of ORR activity and oxygen adsorption strength (E_{OH*}), emphasizes the need for an optimal catalyst—one where the adsorption strength of crucial intermediates strikes a balance between not being too weak or too strong. Interestingly, akin to the case of a clean flat surface, we observed a similar volcano plot for the $M_1O_x(OH)_y$ complexes and metallic $Ag_{54}M_1$ clusters where the ORR activity varied as a function of the OH* adsorption energy (E_{OH*}).[39] The fluxionality of small clusters might challenge the typical ORR volcano curve observed on flat or stepped transition metal surfaces. Nonetheless, our prolonged MDs simulations (2 ns) demonstrate that within the $Ag_{54}M_1O_x(OH)_y$ clusters, atoms largely show localized movements and retain the general cluster structure (Figure S9). The ORR was studied for the $M_1O_x(OH)_y$ complex residing on the $Ag_{54}M_1O_x(OH)_y$ icosahedron cluster while neglecting the flexibility effects of the cluster. Consequently, there are no significant rearrangements throughout the simulation that would result in a deviation from the volcano curve. The left side of the volcano plot represents metals that exhibit weak interactions with OH* (E_{OH*} > 0.1 eV), while the right side

https://doi.org/10.1021/jacsau.4c00116
JACS Au 2024, 4, 2886–2895

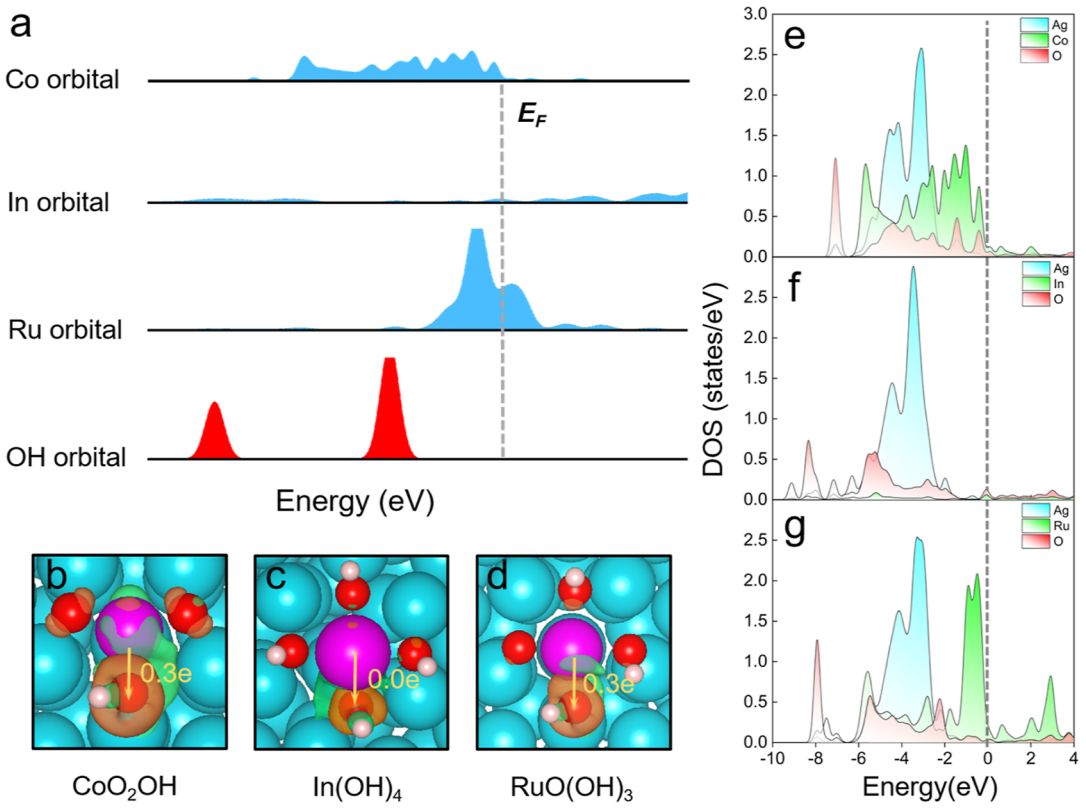

Figure 4. Electron structure analysis of $Ag_{54}M_1O_x(OH)_y$ (M = Ru, Co, and In) cluster catalysts. (a) The calculated orbitals of the OH radical, Co, In, and Ru atoms in the $M_1O_x(OH)_y$ clusters. (b–d) Differential charge density analysis for OH* adsorption in the $Ag_{54}Co_2OH$, $Ag_{54}In_1(OH)_4$, and $Ag_{54}Ru_1O(OH)_3$ clusters. The colors green and pink indicate positive and negative values, respectively, with an isosurface level of 0.004 e/Å^3. (e–g) Density of state analysis for OH* adsorption in the $M_1O_x(OH)_y$ clusters. The blue, white, red, and pink spheres are Ag, H, O, and single metal atoms, respectively.

features metals that strongly interact with OH* (E_{OH*} < 0.1 eV). The peak atop the volcano corresponds to high ORR activity, illustrating that the ideal ORR catalyst is characterized by OH* binding with moderate strength. This balance in the OH* binding strength, positioned at the peak of the E_{OH*} volcano plot, is indicative of an optimal catalyst for the ORR.

Remarkably, the ORR activity varied significantly among the different $Ag_{54}M_1$ clusters, emphasizing the pivotal role of the specific doping of single atoms in fine-tuning the catalytic activity for the ORR. Among these complexes, the Co_1O_2OH complex shows the highest ORR activity, with a high U_L of 0.61 V (Table S9). The Co_1O_2OH complexes show higher activity than the Pt(111) surface, indicating that the $Ag_{54}Co_1$ clusters hold promise as potential candidates for replacing noble Pt catalysts for the ORR in alkaline environments. Moreover, the U_L of $Ag_{54}Au_1(OH)_3$ and $Ag_{54}Pd_1(OH)_3$ (0.65 and 0.59 V) is slightly greater than that of Pt, whereas the SAA $Ag_{54}Ru_1O(OH)_3$ and $Ag_{54}Rh_1O(OH)_3$ clusters have even lower ORR activity, with a U_L of nearly −0.20 V due to the stronger adsorption of *OH intermediates on the latter clusters (Table S9). However, the $Ag_{54}In_1(OH)_4$ cluster also exhibited low ORR activity, with a U_L of 0.31 eV (Table S9), which was attributed to the weak adsorption of OH* on the cluster, resulting in a high energy cost during the formation of crucial OOH* intermediates.

Traditional theoretical modeling often relies on the use of pure metallic cluster alloy models to interpret experimental observations. A comparison of the volcano curves representing the $Ag_{54}M_1O_x(OH)_y$ and $Ag_{54}M_1$ models highlighted significant differences in their catalytic behaviors. However, metallic alloy models frequently fail to accurately represent the ORR activity observed in the experiments. For instance, the metallic $Ag_{54}Au_1$ cluster demonstrates a positive OOH* formation energy (E_{OH*} = 0.50 eV) (Table S8), leading to significantly low ORR activity with a U_L of 0.30 V (Table S9). However, when structured as an $Ag_{54}Au_1O(OH)_2$ cluster, $Au_1O(OH)_2$ exhibited an OOH* formation energy of approximately 0.15 eV, suggesting high ORR activity (U_L = 0.65 V). The $Au_1O(OH)_2$ complex model supports experimental measurements showing the presence of single Au atoms in an oxidized state,[40,41] as indicated in Table S10. This difference in behavior between the operando-formed $Au_1O(OH)_2$ complex and the metallic $Ag_{54}Au_1$ cluster emphasizes the need to identify the true configuration under operando reaction conditions through a comparison between the calculated ORR activity and experimental results. The convergence between the experimental results and calculations strongly indicates that the active species of Ag-based alloy clusters under the reaction conditions is the $Au_1O(OH)_2$ complex with high ORR activity. This new perspective has been further explored in light of experimental findings that demonstrate superior ORR activity in AgCu and AgPd alloy nanoparticle catalysts with Cu and Pd in an oxide state, as reported in several studies.[42−45] However, it is important to note that the $Ag_{54}Pt_1$ alloy shows activity lower than that of the $Ag_{54}Co_1$, $Ag_{54}Cu_1$, and $Ag_{54}Au_1$ clusters. This outstanding performance of AgPt alloys from the experimental data suggested that in addition to the formation of $M_1O_x(OH)_y$ complexes, other unique structural config-

https://doi.org/10.1021/jacsau.4c00116
JACS Au 2024, 4, 2886−2895

urations in Ag-based alloys might contribute to enhanced ORR activity.[46,47] Our findings strengthen our understanding of the role and significance of these complexes formed under operational ORR conditions in dictating the catalytic behavior of these alloys during the ORR process.

To achieve the highest U_L, it is essential to have an appropriate OH* adsorption strength, which is strongly correlated with orbital hybridization between OH* and single-atom M centers in operando-formed $M_1O_x(OH)_y$ complexes. Moderate OH* adsorption necessitates appropriate orbital hybridization between OH* and a single-atom M center. We compared the electronic structures of OH* adsorbed by the $Ag_{54}Co_1O_2OH$, $Ag_{54}In_1(OH)_4$, and $Ag_{54}Ru_1O(OH)_3$ cluster catalysts, which exhibited moderate, weak, and strong adsorption strengths, respectively. The restricted occupancy of 4d orbitals in $Ag_{54}In_1(OH)_4$ leads to much weaker hybridization with OH* and reduced charge transfer from In atoms to OH*, resulting in a significantly lower OH* adsorption strength and ORR activity. On the other hand, the significant expansion of the Ru 4d orbital near the Fermi level and the proximity of the energy levels between the Ru and OH* orbitals led to large charge transfer and strong hybridization, which resulted in strong OH* adsorption at the Ru site (Figure 4a). The crystal orbital Hamilton population (COHP) analysis further corroborates this, showing a greater occupation of the bonding orbitals between Ru and the oxygen atom in OH*, as illustrated in Figure S10. The strong OH* adsorption poisons the Ru site, leading to a reduction in ORR activity. In contrast, the $Ag_{54}Co_1O_2OH$ complex exhibited high ORR activity, primarily attributed to its moderate OH* adsorption strength, moderate electrostatic interactions, and moderate hybridization between Co and OH* (Figures 4a–g and S11, S12). The conjecture that simultaneous hybridization of adsorbates with a single atom in $Ag_{54}M_1O_x(OH)_y$ complexes contributes to high ORR activity is a compelling insight, indicating that such interactions play a crucial role in achieving optimal catalytic behavior.

To illustrate the significant difference in performance between the $Ag_{54}Co_1O_2OH$ and $Ag_{54}Co_1$ cluster models, we conducted further electronic analysis to reveal the greater activity of the $Ag_{54}Co_1O_2OH$ complex compared to that of the metallic $Ag_{54}Co_1$ cluster. The enhanced adsorption of OH* on metallic $Ag_{54}Co_1$ compared to that on the $Ag_{54}Co_1O_2OH$ complex can be attributed to stronger repulsive interactions between OH* and other O* species on the latter complex. On the metallic $Ag_{54}Co_1$ cluster, where Co is positioned on the surface, significant hybridization occurs between Co and OH* at −6.00 eV, but this hybridization is not observed in the case of $Ag_{54}Co_1O_2OH$, as shown in Figure S11. COHP analysis revealed that a greater number of bonding orbitals between Co and O* in OH* are occupied on the $Ag_{54}Co_1$ surface than in the $Ag_{54}Co_1O_2OH$ complex. This leads to a lower integrated ICOHP for the Ag−O bond in the $Ag_{54}Co_1O_2OH$ complex, as demonstrated in Figure S12. As a result, OH* exhibited a moderate adsorption strength on the $Ag_{54}Co_1O_2OH$ complex, in contrast to its stronger adsorption on the metallic $Ag_{54}Co_1$ cluster. This stronger adsorption on metallic $Ag_{54}Co_1$ results in decreased ORR activity due to a poisoning effect on the cluster. Our research emphasizes the importance of considering the operando formation of structures in accurately determining the active site of the ORR.

CONCLUSIONS

In summary, comprehensive first-principles calculations revealed that the $Ag_{54}M_1O_x(OH)_y$ complex acts as the pivotal active site for catalyzing the ORR over Ag-based SAA cluster catalysts. The resulting volcano plot derived for the $Ag_{54}M_1O_x(OH)_y$ complex concurs with the experimental observations, contrasting with the inadequacy of commonly used models for identifying metallic SAA AgM_1 clusters. Our work underscores the importance of theoretical modeling considering the reaction atmosphere in uncovering the true active site of a reaction. These insights deepened our understanding of the structures of the $Ag_{54}M_1O_x(OH)_y$ complex under the ORR conditions, offering valuable perspectives for better catalyst design for the ORR and other catalytic systems.

METHODS

Spin-polarized DFT calculations were conducted by using the Vienna ab initio simulation package (VASP) code.[48,49] We used projector augmented wave potentials[50] and utilized the Perdew−Burke−Ernzerhof functionals.[51] During the cluster calculations, we placed the 55-atom Ag clusters in a vacuum box with cell dimensions of 16.34 × 16.34 × 16.34 Å. The icosahedron Ag_{55} clusters generally exhibit (111)-like surfaces. The Brillouin zone was sampled with a 1 × 1 × 1 Monkhorst-Pack *k*-point. The energy cutoff for the plane wave basis set was set at 350 eV during structure optimization, and the geometry optimization was considered complete when the forces on each atom were less than 0.05 eV/Å with a convergence threshold of 10^{-4} eV. The electronic analysis of the COHP analysis was conducted by using LOBSTER.[52] The VASPKIT package[53] was used for postprocessing the VASP calculations.

We employed well-tempered metadynamics simulation for exploration of the FES. These simulations were conducted using the large-scale atomic/molecular massively parallel simulator (LAMMPS) software,[54] which incorporates the Collective Variables Module (Colvars),[55] to apply the biasing potentials. Energy and force calculations were performed utilizing the NN potential of the Recursively Embedded Atom Neural Network (REANN)[56−58] within LAMMPS. In this study, the neural network architecture comprised layers of 256 and 128 nodes. A cutoff distance of 7 Å was implemented. The orbital count was established at 10, with Gaussian-type orbitals (GTOs) characterized by s, p, and d functions. In this work, 50,000 structures obtained by ab initio MDs simulations[59] were calculated for training the NN potential for the $Ag_{54}M_1O_x$ cluster. The root-mean-square error was 1.54 meV/atom. The AIMD simulations were carried out in the canonical ensemble (*NVT*) at 400 K with a time step of 0.5 fs. More details on the DFT calculations, GCMC simulations, and establishment of the Pourbaix diagram are provided in the Supporting Information.

ASSOCIATED CONTENT

Data Availability Statement

The data that support the findings of this study are available from the corresponding author upon reasonable request.

Supporting Information

The Supporting Information is available free of charge at https://pubs.acs.org/doi/10.1021/jacsau.4c00116.

Detailed methodology, GCMC simulations, and Pourbaix diagrams (PDF)

AUTHOR INFORMATION

Corresponding Author

Jin-Xun Liu − *Key Laboratory of Precision and Intelligent Chemistry, School of Chemistry and Materials Science,*

https://doi.org/10.1021/jacsau.4c00116
JACS Au 2024, 4, 2886−2895

University of Science and Technology of China, Hefei, Anhui 230026, China; Hefei National Laboratory, University of Science and Technology of China, Hefei 230088, China; orcid.org/0000-0002-7499-4197; Email: jxliu86@ustc.edu.cn

Authors

Yixuan Pu − *Key Laboratory of Precision and Intelligent Chemistry, School of Chemistry and Materials Science, University of Science and Technology of China, Hefei, Anhui 230026, China*

Jia-Lan Chen − *Key Laboratory of Precision and Intelligent Chemistry, School of Chemistry and Materials Science, University of Science and Technology of China, Hefei, Anhui 230026, China*

Jian-Wen Zhao − *Key Laboratory of Precision and Intelligent Chemistry, School of Chemistry and Materials Science, University of Science and Technology of China, Hefei, Anhui 230026, China*

Li Feng − *Key Laboratory of Precision and Intelligent Chemistry, School of Chemistry and Materials Science, University of Science and Technology of China, Hefei, Anhui 230026, China*

Jinze Zhu − *Key Laboratory of Precision and Intelligent Chemistry, School of Chemistry and Materials Science, University of Science and Technology of China, Hefei, Anhui 230026, China*

Xuechun Jiang − *Key Laboratory of Precision and Intelligent Chemistry, School of Chemistry and Materials Science, University of Science and Technology of China, Hefei, Anhui 230026, China*

Wei-Xue Li − *Key Laboratory of Precision and Intelligent Chemistry, School of Chemistry and Materials Science, University of Science and Technology of China, Hefei, Anhui 230026, China; Hefei National Laboratory, University of Science and Technology of China, Hefei 230088, China*

Complete contact information is available at: https://pubs.acs.org/10.1021/jacsau.4c00116

Author Contributions

[§]Y.P. and J.-L.C. authors contributed equally. J.X.L. conceived the idea and supervised and directed the project. Y.P. performed the theoretical calculations and analyzed the DFT data. All the authors discussed the results and wrote and commented on the paper. CRediT: **Yixuan Pu** conceptualization, formal analysis, investigation, writing-original draft, writing-review & editing; **Jia-Lan Chen** conceptualization, formal analysis, investigation, writing-review & editing; **Jian-Wen Zhao** formal analysis, methodology, writing-original draft, writing-review & editing; **Li Feng** data curation, investigation, writing-review & editing; **Jinze Zhu** formal analysis, investigation; **Xuechun Jiang** formal analysis, investigation, writing-review & editing; **Wei-Xue Li** formal analysis, investigation; **Jin-Xun Liu** conceptualization, project administration, supervision, writing-review & editing.

Notes

The authors declare no competing financial interest.

■ ACKNOWLEDGMENTS

This work was supported by the Key Technologies R&D Program of China (2021YFA1502804), the Strategic Priority Research Program of the Chinese Academy of Science (XDB0450102), the National Natural Science Foundation of China (22172150, 22221003, and 22222306), the National Natural Science Foundation of Anhui Province (2108085QB62), the USTC Research Funds of the Double First-Class Initiative (YD2060002012), K. C. Wong Education (GJTD-2020-15), the Innovation Program for Quantum Science and Technology (2021ZD0303302), and high-performance computational resources provided by the University of Science and Technology of China and the Hefei Advanced Computing Center.

■ REFERENCES

(1) Ali, A.; Khandelwal, S.; Panja, S.; Majumder, P.; Dutta, A. Oxygen reduction reaction in nature and its importance in life. In *Oxygen Reduction Reaction*; Elsevier, 2022; pp 1−43.

(2) Liu, M.; Xiao, X.; Li, Q.; Luo, L.; Ding, M.; Zhang, B.; Li, Y.; Zou, J.; Jiang, B. Recent progress of electrocatalysts for oxygen reduction in fuel cells. *J. Colloid Interface Sci.* **2022**, *607*, 791−815.

(3) Spendelow, J. S.; Wieckowski, A. Electrocatalysis of oxygen reduction and small alcohol oxidation in alkaline media. *Phys. Chem. Chem. Phys.* **2007**, *9* (21), 2654.

(4) Li, Y.; Dai, H. Recent advances in zinc-air batteries. *Chem. Soc. Rev.* **2014**, *43* (15), 5257−5275.

(5) Pei, P.; Wang, K.; Ma, Z. Technologies for extending zinc−air battery's cyclelife: A review. *Appl. Energy* **2014**, *128*, 315−324.

(6) Neburchilov, V.; Wang, H.; Martin, J. J.; Qu, W. A review on air cathodes for zinc−air fuel cells. *J. Power Sources* **2010**, *195* (5), 1271−1291.

(7) Wang, X. X.; Sokolowski, J.; Liu, H.; Wu, G. Pt alloy oxygen-reduction electrocatalysts: Synthesis, structure, and property. *Chin. J. Catal.* **2020**, *41* (5), 739−755.

(8) Greeley, J.; Stephens, I. E.; Bondarenko, A. S.; Johansson, T. P.; Hansen, H. A.; Jaramillo, T. F.; Rossmeisl, J.; Chorkendorff, I.; Norskov, J. K. Alloys of platinum and early transition metals as oxygen reduction electrocatalysts. *Nat. Chem.* **2009**, *1* (7), 552−556.

(9) Kodama, K.; Nagai, T.; Kuwaki, A.; Jinnouchi, R.; Morimoto, Y. Challenges in applying highly active Pt-based nanostructured catalysts for oxygen reduction reactions to fuel cell vehicles. *Nat. Nanotechnol.* **2021**, *16* (2), 140−147.

(10) Wang, X.; Li, Z.; Qu, Y.; Yuan, T.; Wang, W.; Wu, Y.; Li, Y. Review of Metal Catalysts for Oxygen Reduction Reaction: From Nanoscale Engineering to Atomic Design. *Chem* **2019**, *5* (6), 1486−1511.

(11) Chandran, P.; Ghosh, A.; Ramaprabhu, S. High-performance Platinum-free oxygen reduction reaction and hydrogen oxidation reaction catalyst in polymer electrolyte membrane fuel cell. *Sci. Rep.* **2018**, *8* (1), 3591.

(12) Gates, B. C.; Katz, A.; Liu, J. Nested Metal Catalysts: Metal Atoms and Clusters Stabilized by Confinement with Accessibility on Supports. *Precis. Chem.* **2023**, *1* (1), 3−13.

(13) Holewinski, A.; Idrobo, J. C.; Linic, S. High-performance Ag-Co alloy catalysts for electrochemical oxygen reduction. *Nat. Chem.* **2014**, *6* (9), 828−834.

(14) Balkan, T.; Küçükkeçeci, H.; Aksoy, D.; Harfouche, M.; Metin, O.·.; Kaya, S. Ag/AgCl clusters derived from AgCu alloy nanoparticles as electrocatalysts for the oxygen reduction reaction. *Sustainable Energy Fuels* **2022**, *6* (10), 2593−2601.

(15) Bhatt, M. D.; Lee, G.; Lee, J. S. Screening of Oxygen-Reduction-Reaction-Efficient Electrocatalysts Based on Ag−M (M = 3d, 4d, and 5d Transition Metals) Nanoalloys: A Density Functional Theory Study. *Energy Fuels* **2017**, *31* (2), 1874−1881.

(16) Hannagan, R. T.; Giannakakis, G.; Flytzani-Stephanopoulos, M.; Sykes, E. C. H. Single-Atom Alloy Catalysis. *Chem. Rev.* **2020**, *120* (21), 12044−12088.

(17) Greiner, M. T.; Jones, T. E.; Beeg, S.; Zwiener, L.; Scherzer, M.; Girgsdies, F.; Piccinin, S.; Armbruster, M.; Knop-Gericke, A.; Schlogl, R. Free-atom-like d states in single-atom alloy catalysts. *Nat. Chem.* **2018**, *10* (10), 1008−1015.

(18) Liu, W.; Feng, H.; Yang, Y.; Niu, Y.; Wang, L.; Yin, P.; Hong, S.; Zhang, B.; Zhang, X.; Wei, M. Highly-efficient RuNi single-atom alloy catalysts toward chemoselective hydrogenation of nitroarenes. *Nat. Commun.* **2022**, *13* (1), 3188.
(19) Zhang, T.; Walsh, A. G.; Yu, J.; Zhang, P. Single-atom alloy catalysts: structural analysis, electronic properties and catalytic activities. *Chem. Soc. Rev.* **2021**, *50* (1), 569−588.
(20) Han, Z. K.; Sarker, D.; Ouyang, R.; Mazheika, A.; Gao, Y.; Levchenko, S. V. Single-atom alloy catalysts designed by first-principles calculations and artificial intelligence. *Nat. Commun.* **2021**, *12* (1), 1833.
(21) Mao, J.; Yin, J.; Pei, J.; Wang, D.; Li, Y. Single atom alloy: An emerging atomic site material for catalytic applications. *Nano Today* **2020**, *34*, 100917.
(22) Feng, H.; Zhang, M.; Ge, Z.; Deng, Y.; Pu, P.; Zhou, W.; Yuan, H.; Yang, J.; Li, F.; Zhang, X.; et al. Designing Efficient Single-Atom Alloy Catalysts for Selective C=O Hydrogenation: A First-Principles, Active Learning and Microkinetic Study. *ACS Appl. Mater. Interfaces* **2023**, *15* (48), 55903−55915.
(23) Chen, L.; Qi, Z.; Peng, X.; Chen, J. L.; Pao, C. W.; Zhang, X.; Dun, C.; Young, M.; Prendergast, D.; Urban, J. J.; et al. Insights into the Mechanism of Methanol Steam Reforming Tandem Reaction over CeO(2) Supported Single-Site Catalysts. *J. Am. Chem. Soc.* **2021**, *143* (31), 12074−12081.
(24) Zhang, Y.; Shi, X.-R.; Sun, C.; Huang, S.; Duan, Z.; Ma, P.; Wang, J. CO oxidation on Ni-based single-atom alloys surfaces. *Mol. Catal.* **2020**, *495*, 111154.
(25) Hannagan, R. T.; Giannakakis, G.; Réocreux, R.; Schumann, J.; Finzel, J.; Wang, Y.; Michaelides, A.; Deshlahra, P.; Christopher, P.; Flytzani-Stephanopoulos, M.; et al. First-principles design of a single-atom−alloy propane dehydrogenation catalyst. *Science* **2021**, *372* (6549), 1444−1447.
(26) Zhang, L.; Liu, H.; Liu, S.; Norouzi Banis, M.; Song, Z.; Li, J.; Yang, L.; Markiewicz, M.; Zhao, Y.; Li, R.; et al. Pt/Pd Single-Atom Alloys as Highly Active Electrochemical Catalysts and the Origin of Enhanced Activity. *ACS Catal.* **2019**, *9* (10), 9350−9358.
(27) Niu, X.; Wei, J.; Xu, D.; Pei, J.; Sui, R. Charge-asymmetry Fe1Cu single atom alloy catalyst for efficient oxygen reduction reaction. *Nano Res.* **2024**, *17*, 4702−4710.
(28) Darby, M. T.; Stamatakis, M. Single-Atom Alloys for the Electrochemical Oxygen Reduction Reaction. *ChemPhysChem* **2021**, *22* (5), 499−508.
(29) Zou, X.; He, S.; Kang, X.; Chen, S.; Yu, H.; Jin, S.; Astruc, D.; Zhu, M. New atomically precise M1Ag21 (M = Au/Ag) nanoclusters as excellent oxygen reduction reaction catalysts. *Chem. Sci.* **2021**, *12* (10), 3660−3667.
(30) Adnan, Q.; Fuyi, C.; Nan, Z. Ag−Cu Nanoalloy Electrocatalysts for Oxygen Reduction in Alkaline Media for Advanced Energy Conversion and Storage. In *Advanced Catalytic Materials*; Luis Enrique, N., Jin-An, W., Eds.; IntechOpen, 2016; Ch. 15
(31) Lei, Y.; Chen, F.; Jin, Y.; Liu, Z. Ag-Cu nanoalloyed film as a high-performance cathode electrocatalytic material for zinc-air battery. *Nanoscale Res. Lett.* **2015**, *10* (1), 197.
(32) Shin, K.; Kim, D. H.; Yeo, S. C.; Lee, H. M. Structural stability of AgCu bimetallic nanoparticles and their application as a catalyst: A DFT study. *Catal. Today* **2012**, *185* (1), 94−98.
(33) Minamihara, H.; Kusada, K.; Wu, D.; Yamamoto, T.; Toriyama, T.; Matsumura, S.; Kumara, L. S. R.; Ohara, K.; Sakata, O.; Kawaguchi, S.; et al. Continuous-Flow Reactor Synthesis for Homogeneous 1 nm-Sized Extremely Small High-Entropy Alloy Nanoparticles. *J. Am. Chem. Soc.* **2022**, *144* (26), 11525−11529.
(34) Ouyang, R. H.; Liu, J. X.; Li, W. X. Atomistic Theory of Ostwald Ripening and Disintegration of Supported Metal Particles under Reaction Conditions. *J. Am. Chem. Soc.* **2013**, *135* (5), 1760−1771.
(35) Hansen, H. A.; Rossmeisl, J.; Nørskov, J. K. Surface Pourbaix diagrams and oxygen reduction activity of Pt, Ag and Ni(111) surfaces studied by DFT. *Phys. Chem. Chem. Phys.* **2008**, *10* (25), 3722−3730.
(36) Wang, Z.; Guo, X.; Montoya, J.; Nørskov, J. K. Predicting aqueous stability of solid with computed Pourbaix diagram using SCAN functional. *npj Comput. Mater.* **2020**, *6* (1), 160.
(37) Zhao, Y.; Adiyeri Saseendran, D. P.; Huang, C.; Triana, C. A.; Marks, W. R.; Chen, H.; Zhao, H.; Patzke, G. R. Oxygen Evolution/Reduction Reaction Catalysts: From In Situ Monitoring and Reaction Mechanisms to Rational Design. *Chem. Rev.* **2023**, *123* (9), 6257−6358.
(38) Ge, X.; Sumboja, A.; Wuu, D.; An, T.; Li, B.; Goh, F. W. T.; Hor, T. S. A.; Zong, Y.; Liu, Z. Oxygen Reduction in Alkaline Media: From Mechanisms to Recent Advances of Catalysts. *ACS Catal.* **2015**, *5* (8), 4643−4667.
(39) Kulkarni, A.; Siahrostami, S.; Patel, A.; Norskov, J. K. Understanding Catalytic Activity Trends in the Oxygen Reduction Reaction. *Chem. Rev.* **2018**, *118* (5), 2302−2312.
(40) Nandy, A.; De, S. K.; Mishra, S. M.; Satpati, B.; Paul, M.; Mukhopadhyay, M. K.; Senapati, D. Ag@AuAg@Ag Nanocatalyst for the Electrocatalytic Oxygen Reduction Reaction. *ACS Appl. Nano Mater.* **2024**, *7* (13), 14889−14897.
(41) Qaseem, A.; Chen, F.; Wu, X.; Johnston, R. L. Pt-free silver nanoalloy electrocatalysts for oxygen reduction reaction in alkaline media. *Catal. Sci. Technol.* **2016**, *6* (10), 3317−3340.
(42) Balkan, T.; Küçükkeçeci, H.; Zarenezhad, H.; Kaya, S.; Metin, O. ·. One-pot synthesis of monodisperse copper−silver alloy nanoparticles and their composition-dependent electrocatalytic activity for oxygen reduction reaction. *J. Alloys Compd.* **2020**, *831*, 154787.
(43) Slanac, D. A.; Hardin, W. G.; Johnston, K. P.; Stevenson, K. J. Atomic Ensemble and Electronic Effects in Ag-Rich AgPd Nanoalloy Catalysts for Oxygen Reduction in Alkaline Media. *J. Am. Chem. Soc.* **2012**, *134* (23), 9812−9819.
(44) Ashok, A.; Kumar, A.; Matin, M. A.; Tarlochan, F. Probing the effect of combustion controlled surface alloying in silver and copper towards ORR and OER in alkaline medium. *J. Electroanal. Chem.* **2019**, *844*, 66−77.
(45) Santoveña-Uribe, A.; Maya-Cornejo, J.; Bahena, D.; Ledesma, J.; Pérez, R.; Esparza, R. Synthesis and Characterization of AgPd Bimetallic Nanoparticles as Efficient Electrocatalysts for Oxygen Reduction Reaction. *Electrocatalysis* **2020**, *11* (5), 536−545.
(46) Cao, J.; Guo, M.; Wu, J.; Xu, J.; Wang, W.; Chen, Z. Carbon-supported Ag@ Pt core−shell nanoparticles with enhanced electrochemical activity for methanol oxidation and oxygen reduction reaction. *J. Power Sources* **2015**, *277*, 155−160.
(47) Aksoy, D.; Karakaya, C.; Balkan, T.; Savaci, U.; Turan, S.; Metin, O. ·.; Kaya, S. Controlling Oxygen Reduction Reaction Activities of Ag@ Pt Core−Shell Nanoparticles Via Tuning of Ag in the Surface Layer. *Energy Technol.* **2023**, *11* (4), 2201167.
(48) Kresse, G.; Hafner, J. Ab initiomolecular dynamics for liquid metals. *Phys. Rev. B: Condens. Matter Mater. Phys.* **1993**, *47* (1), 558−561.
(49) Kresse, G.; Furthmüller, J. Efficient iterative schemes for ab initio total-energy calculations using a plane-wave basis set. *Phys. Rev. B: Condens. Matter Mater. Phys.* **1996**, *54* (16), 11169−11186.
(50) Blochl, P. E. Projector augmented-wave method. *Phys. Rev. B: Condens. Matter Mater. Phys.* **1994**, *50* (24), 17953−17979.
(51) Perdew, J. P.; Burke, K.; Ernzerhof, M. Generalized gradient approximation made simple. *Phys. Rev. Lett.* **1996**, *77* (18), 3865−3868.
(52) Dronskowski, R.; Bloechl, P. E. Crystal orbital Hamilton populations (COHP): energy-resolved visualization of chemical bonding in solids based on density-functional calculations. *J. Phys. Chem.* **1993**, *97* (33), 8617−8624.
(53) Wang, V.; Xu, N.; Liu, J.-C.; Tang, G.; Geng, W.-T. VASPKIT: A user-friendly interface facilitating high-throughput computing and analysis using VASP code. *Comput. Phys. Commun.* **2021**, *267*, 108033.
(54) Thompson, A. P.; Aktulga, H. M.; Berger, R.; Bolintineanu, D. S.; Brown, W. M.; Crozier, P. S.; in 't Veld, P. J.; Kohlmeyer, A.; Moore, S. G.; Nguyen, T. D.; et al. LAMMPS - a flexible simulation

https://doi.org/10.1021/jacsau.4c00116
JACS Au 2024, 4, 2886−2895

tool for particle-based materials modeling at the atomic, meso, and continuum scales. *Comput. Phys. Commun.* **2022**, *271*, 108171.
(55) Fiorin, G.; Klein, M. L.; Hénin, J. Using collective variables to drive molecular dynamics simulations. *Mol. Phys.* **2013**, *111* (22−23), 3345−3362.
(56) Zhang, Y.; Xia, J.; Jiang, B. REANN: A PyTorch-based end-to-end multi-functional deep neural network package for molecular, reactive, and periodic systems. *J. Chem. Phys.* **2022**, *156* (11), 114801.
(57) Zhang, Y.; Xia, J.; Jiang, B. Physically Motivated Recursively Embedded Atom Neural Networks: Incorporating Local Completeness and Nonlocality. *Phys. Rev. Lett.* **2021**, *127* (15), 156002.
(58) Zhang, Y.; Hu, C.; Jiang, B. Embedded Atom Neural Network Potentials: Efficient and Accurate Machine Learning with a Physically Inspired Representation. *J. Phys. Chem. Lett.* **2019**, *10* (17), 4962−4967.
(59) Pastore, G.; Smargiassi, E.; Buda, F. Theory of ab initio molecular-dynamics calculations. *Phys. Rev. A* **1991**, *44* (10), 6334−6347.

https://doi.org/10.1021/jacsau.4c00116
JACS Au 2024, 4, 2886−2895